Materials Science & Engineering A 868 (2023) 144761

Contents lists available at ScienceDirect

Materials Science & Engineering A

journal homepage: www.elsevier.com/locate/msea

Breaking strength-ductility trade-off in laser-powder bed fused Fe–Cr–Ni–Al maraging stainless steel: Controlled precipitation and preserved dislocations

Richard Fabian, Amir Hadadzadeh *

Department of Mechanical Engineering, University of Memphis, Memphis, TN, USA

ARTICLE INFO

Keywords:
Laser-powder bed fusion
Maraging steel
Precipitation kinetics
Dislocation
Strength
Ductility

ABSTRACT

In the current study, cylindrical rods of Fe–Cr–Ni–Al maraging steel (with the brand name CX) are fabricated using the laser-powder bed fusion (L-PBF) technique. The material is analyzed using the differential scanning calorimetry (DSC) technique under continuous heating at different heating rates. The DSC results are employed to identify the heat flow peaks associated with the precipitation and austenite reversion phase transformations. The peaks are then analyzed and processed to determine the onset, peak, and end temperatures associated with each phase transformation. These results are used to calculate the degree of phase transformation under non-isothermal conditions and to evaluate the activation energy of transformation through the Kissinger method. In the next step, the modified Johnson-Mehl-Avrami-Kolmogorov (JMAK) model is employed to model the kinetics of phase transformations during non-isothermal heating. The validated model is then used to predict the kinetics of precipitation and austenite reversion phase transformations under isothermal aging heat treatments. The isothermal modeling results are employed to design a direct aging heat treatment to promote the evolution of nanometric β-NiAl precipitates and meanwhile preserve the pre-existing dislocation networks. Such a heat treatment results in the enhancement of both yield and tensile strengths from 929 MPa and 1032 MPa in the as-built condition to 1659 MPa and 1738 MPa after heat treatment. Meanwhile, ductility slightly changes from 15.3% in the as-built condition to 14.7% after heat treatment. Such an achievement in breaking the strength-ductility trade-off is due to a controlled heat treatment process that preserves the dislocation networks.

1. Introduction

Precipitation-hardenable (PH) stainless steels are of particular interest for applications under severe service conditions such as load-bearing at high temperatures, and corrosive environments. Therefore, they possess vast applications in advanced industries such as aerospace, marine, and nuclear [1,2]. PH stainless steels have significantly higher strength than ferritic or austenitic stainless steels [3]. Meanwhile, these steels possess good ductility and toughness [4]. Different classes of PH stainless steels have been developed by changing the chemistry and the resulting precipitates and properties. Some examples include PH 13-8 Mo, PH 17–4, and PH 15–5. Among these alloys, PH 13-8 Mo possesses superior mechanical properties compared to other types [5].

In the case of the existence of a martensitic microstructure, similar to the microstructure of PH 13-8 Mo, the steel is called maraging stainless steel since maraging is a portmanteau of “martensite” and “aging”. The aging heat treatment process results in the evolution of precipitates. PH 13-8 Mo consists of a ductile martensitic matrix, strengthened by the evolution of nanoscaled precipitates [6]. Unlike conventional PH and maraging steels where the strength is enhanced by the evolution of Cu-rich, Nb-rich, and/or Ni_3Ti particles [7], the strengthening precipitate in the PH 13-8 Mo steel is β-NiAl with an ordered CsCl structure [8,9]. NiAl precipitates are one of the most effective intermetallic phases to strengthen the maraging steels [1,10,11] due to their lattice constant of 2.8752 ± 0.0004 Å which is close to that of the ferritic steel (α-Fe, bcc); 2.8829 ± 0.0002 Å [12]. As a result, a minimal lattice misfit between the precipitates and the matrix is achieved which will then enhances the strength through the chemical ordering effect and the creation of backstresses (the forces that oppose the dislocation motion) [13].

The importance of maraging steels in different industries makes it imperative to study their additive manufacturing (AM) since metal AM processes have been emerging in these industries as revolutionary

* Corresponding author.
E-mail address: amir.hadadzadeh@memphis.edu (A. Hadadzadeh).

https://doi.org/10.1016/j.msea.2023.144761
Received 19 December 2022; Received in revised form 6 February 2023; Accepted 8 February 2023
Available online 10 February 2023

manufacturing techniques [14]. The reason for identifying the metal AM processes as revolutionary manufacturing techniques is due to their capability to fabricate near-net-shape, complex-shaped, and on-demand components, directly from a feedstock (usually wire or powder). In most of the metal AM processes, the fabrication of the components is accomplished by melting the successive layers of feedstock material and joining them on top of each other [15]. The melting process is performed by employing a high-power energy source; in many cases either a laser beam or an electron beam [14,16]. Metal AM processes are classified into two main groups: directed energy deposition (DED) and powder bed fusion (PBF) [17]. Considering the most common energy sources (*i.e.* laser (L) and electron beam (EB)), the main AM processes for metallic materials can be categorized as L-PBF, EB-PBF, L-DED, and EB-DED [17]. Among these methods, L-PBF has shown a promising trend due to its capability to fabricate metallic components with enhanced properties. The enhanced properties are mainly achieved as a result of tailoring ultrafine, metastable, and hierarchical microstructures using the L-PBF process [18–21]. Such microstructures develop due to the very high solidification cooling rates (in the range of 10^3–10^8 K/s) during the L-PBF process [15,22].

EOS GmbH has developed a low carbon Fe–Cr–Ni–Al maraging stainless steel powder in the family of PH 13-8 Mo [23] which can be used for the L-PBF fabrication. Some studies have been conducted on the L-PBF of CX steel in the as-built condition. Asgari and Mohammadi [24] fabricated L-PBF-CX components and studied the microstructure and mechanical properties in the as-built condition. They showed that dense L-PBF-CX parts with the least amount of defects could be fabricated and the yield strength (YS) and ultimate tensile strength (UTS) in the as-build condition can reach 1036 MPa and 1113 MPa, respectively. Saby et al. [25] reported the hardness of as-built L-PBF-CX as ~33HRC. Sanjari et al. [26], Shahriari et al. [27], and Pirgazi et al. [28] investigated the microstructure of the L-PBF-CX components with different geometries in the as-built condition. They reported a lath martensitic structure along with retained austenite, in the as-built condition. Both martensite lath size and retained austenite amount, and consequently, the mechanical properties changed by changing the geometry of the samples.

Since CX is a heat treatable steel, the feedstock vendor has suggested the following recipe as a generic treatment for precipitation hardening: austenitization at 900 °C for 1 h followed by rapid air cooling and aging at 530 °C for 3 h [23]. Some researchers have followed the exact procedure and others have conducted a different version of the heat treatment. Table 1 summarizes different heat treatments employed for the L-PBF-CX and the resulting strength and elongation to fracture. Elongation to fracture represents the material's ductility.

Referring to Table 1, strength enhancement after heat treatment is accompanied by ductility loss, which is a common phenomenon in the field of materials science and engineering and is known as the strength-ductility trade-off. In addition, a range of strengths and ductilities has been reported for the heat-treated L-PBF-CX. Two reasons could have caused such variations; different heat treatment recipes and different starting microstructures. Various process parameters have been employed in the available studies to print the CX components with different geometries. It is well-established that changing the process parameters and sample geometry will affect the thermal boundaries during solidification which will then change the thermal history and the resulting microstructure [14,41]. In the case of L-PBF-CX, Sanjari et al. [26,42] showed that printing cuboid, vertical rod, and horizontal rod would substantially affect the microstructure in terms of lath martensite size, retained austenite amount, and texture. Hadadzadeh et al. [43] investigated the response of the cuboid L-PBF-CX to the standard austenitization-aging heat treatment. They observed that such a heat treatment would not result in the evolution of the β-NiAl precipitates and strength enhancement. In fact, the austenitization heat treatment substantially changed the microstructure (*i.e.* martensite lath growth and dislocation annihilation) and retarded the precipitation. On the other hand, direct aging of the as-built cuboid samples resulted in the evolution of nanometric β-NiAl precipitates and hardness enhancement. Meanwhile, the lath martensitic structure was refined due to the rearrangement of the dislocations and recovery, rather than dislocation annihilation. Considering these observations, it is obvious that the precipitation kinetics and the resulting strength are very sensitive to the starting microstructure. In addition, sophisticated microstructural changes occur in the L-PBF-CX during the aging heat treatment that can deteriorate the final strength. It is very important to preserve the dislocations during the heat treatment process since the dislocation networks in the L-PBF alloys can substantially increase both strength and ductility [21]. Therefore, it is essential to conduct a systematic study on the kinetics of precipitation formation and austenite reversion in L-PBF-CX. In a recent study, Shahriari et al. [44] conducted dilatometry on the L-PBF-CX at different heating rates to determine the transformation temperatures (*i.e.* precipitation and austenite reversion). However, they did not model the kinetics of these phase transformations.

In the current study, the kinetics of precipitation and austenite reversion phase transformations in an L-PBF-CX is studied using the differential scanning calorimetry (DSC) technique. DSC is a reliable and precise technique to determine the characteristics of phase transformations in terms of the reaction's enthalpy and transition temperatures [45]. Some studies have been conducted on the DSC of L-PBF maraging steels to determine the onset and end temperatures of precipitation reactions [46,47], however, none of them was dedicated to the modeling of the phase transformation kinetics. Since the microstructure of L-PBF alloys is different from the conventionally fabricated counterparts [14], their physical properties are also different [48]. Therefore, it is essential to consider the role of microstructure in the

Table 1
Summary of the heat treatment procedures employed for L-PBF-CX and the resulting strength and elongation to fracture (YS: yield strength, TS: tensile strength, El: elongation to fracture).

Heat Treatment		As-Built			Heat-Treated			Reference
Austenitization	Aging	YS (MPa)	TS (MPa)	El (%)	YS (MPa)	TS (MPa)	El (%)	
850 °C/30min	525 °C/4 h	–	–	–	1600	1720	1.7	[29]
		–	–	–	1560[a]	1650[a]		[30]
		–	–	–	1640[b]	1700[b]		
		–	–	–	1600	1700		[31]
900 °C/1 h	530 °C/3 h	992	1058	18.4	1563	1683	8.4	[32]
900 °C/1 h	530 °C/3 h	694	1043	16.3	1528	1601	7.3	[33–37]
–		694	1043	–	1395	1510	9.3	
850 °C/30min	525 °C/2 h	1006[a]	1170[a]	16.6[a]	1533[a]	1680[a]	11.2[a]	[38–40]
		919[b]	1090[b]	10.5[b]	1600[b]	1683[b]	5.9[b]	

[a] Horizontally-built.
[b] Vertically-built.

kinetics of phase transformation when a heat treatment is formulated. To the best of our knowledge, no kinetics modeling is available for the precipitation phase transformation in the L-PBF maraging steels. Likewise, the available heat treatment recipe(s) for L-PBF maraging steels seem to be developed by either adopting the recipes for the conventionally-fabricated counterparts or trial-and-error approaches. In both cases, the desired properties are not guaranteed. We believe the novelty of our work lies within our systematic approach to modeling the kinetics of phase transformation, using the kinetics modeling results to formulate the heat treatment, and heat treating the material to preserve the L-PBF microstructural features. Cylindrical rods of CX are fabricated using an EOS M290 machine. The samples are then characterized by employing the DSC technique to determine the onset and end temperatures of the precipitation and austenite reversion phase transformations. The kinetics of phase transformation is then modeled under non-isothermal and isothermal conditions using the modified Johnson-Mehl-Avrami-Kolmogorov (JMAK) model. The modeling results are then validated against experimental observations. The modeling results are also used to design a direct aging heat treatment to enhance the strength of the material at minimal ductility loss. These findings will pave the pathway toward optimum post-process heat treatments to obtain the desired strength-ductility balance in L-PBF precipitation-hardenable steels.

2. Experimental procedure

2.1. Materials and L-PBF process

Cylindrical rods of CX alloy were printed through the L-PBF technique using an EOS M290 machine. The nominal composition of the CX powder was Fe-12 *wt%* Cr-9.2 *wt%* Ni-1.6 *wt%* Al-1.4 *wt%* Mo-0.05 *wt%* C, with an average particle size of 37.5 ± 16 μm [24]. The rods were 12 mm in diameter and 120 mm in length, printed in a vertical configuration as shown schematically in Fig. 1. The process parameters were selected based on the optimum ones recommended by EOS GmbH to yield the least defects. The important process parameters included laser power (P), scan speed (v), hatch distance (l), and layer thickness (h). In the current study, they were set as $P = 258.7$ W, $v = 1067$ mm/s, $l = 100$ μm, and $h = 30$ μm. The laser spot size was 100 μm, and the process was completed under an Ar atmosphere with a controlled oxygen content, held at <0.1%. It should be noted that oxygen pickup during the L-PBF process is very minimal due to the protective argon atmosphere [49], therefore, in our analysis in this paper oxygen did not have a significant role. The rods were then cut from the build plate using the wire EDM technique and used for the rest of the study in the as-built condition.

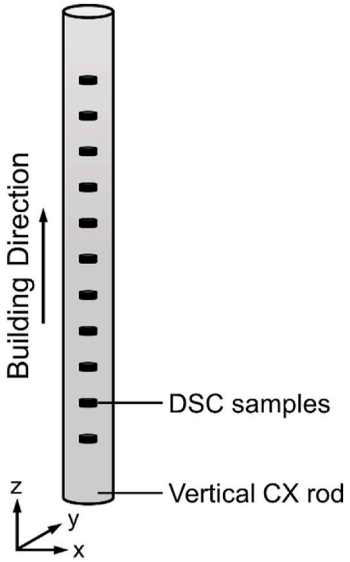

Fig. 1. Schematic of a vertical L-PBF-CX rod along with the DSC samples.

2.2. Differential scanning calorimetry (DSC) analysis

To study the phase transformations in the as-built L-PBF-CX rods, DSC tests were performed using SDT 650-TA Instruments (Delaware, USA). Small discs with the dimensions of 4 mm in diameter and 2 mm in height, were machined from the as-built rods, as shown in Fig. 1. These discs were then used for the DSC analyses. The samples were machined along the centerline of the rods, away from the bottom and top to ensure the consistency of the microstructure and chemistry. Since the microstructure and chemistry are consistent in horizontal rods printed using the EOS M290 machine [49,50], the DSC results were consistent and repeatable. Each DSC trial was repeated 5 times and for each trial, a new as-built sample was used. Each DSC curve was evaluated and the characteristics (*i.e.,* onset, peak, and end temperatures) were reported as an average of the 5 trials. The DSC curves reported in the paper are representative ones. The DSC runs were performed under various heating rates of $\Phi = 5$, 10, 20, 30, 40, and 50 °C/min to a maximum temperature of 1000 °C. The DSC curves of 5 and 10 °C/min heating rates were excluded from further analyses since the peaks were weak and it was not possible to determine the onset and end temperatures accurately. Such a challenge is a common issue with low heating rates and has been reported previously [51]. All the DSC tests were performed under 99.999% argon which flowed throughout the run at 100 mL/min. The DSC curves were then analyzed to identify the exothermic and endothermic reactions that occur in the material.

2.3. Mechanical and microstructural characterization

A Wilson Rockwell hardness tester with a diamond indenter under 150 kgf load and a dwell time of 5s were used to measure the hardness of the as-built and heat-treated specimens. Tensile testings were conducted following the ASTM E8/E8M-21. Dogbone samples with a gauge length of 15.5 mm and a diameter of 6 mm were machined from the rods and tested using an Instron 8800 Uniaxial Servohydraulic System. The tensile tests were conducted under the displacement-controlled condition using an MTS extensometer with a speed of 0.05 mm/min.

Thin films for TEM were prepared using the focused ion beam (FIB) lift-out approach by employing a Thermo Scientific Helios 5 UC DualBeam, as shown in Fig. 2. With an X-FEG source and a high tension adjustable from 80 to 200 kV, TEM studies were carried out using the Thermo Scientific Talos 200X. This system was configured with four in-column SDD Super-X detectors for energy-dispersive X-ray spectroscopy (EDS) signal detection and compositional mapping of the samples.

3. Results

3.1. DSC curves

Fig. 3 shows the representative DSC curves of L-PBF-CX at different heating rates. The DSC curves are reported in terms of normalized heat flow (W/g) with respect to both temperature and time. It is obvious that by increasing the heating rate, the process is completed over a shorter time. The DSC curves are featured by various endothermic and exothermic peaks, indicating the solid-state phenomena/phase transformations in the material. In the current study, two major peaks are considered for further analyses; the exothermic peak over the temperature range of ~410°C–610 °C and the endothermic peak over the temperature range of ~615°C–760 °C. The former represents the precipitation and the latter represents austenite reversion [44]. The reason for considering these two phenomena is the fact that while precipitation significantly enhances the strength of the L-PBF-CX, austenite reversion negatively affects the strength [43]. Since the onset temperature of austenite reversion is very close to the end temperature of precipitation,

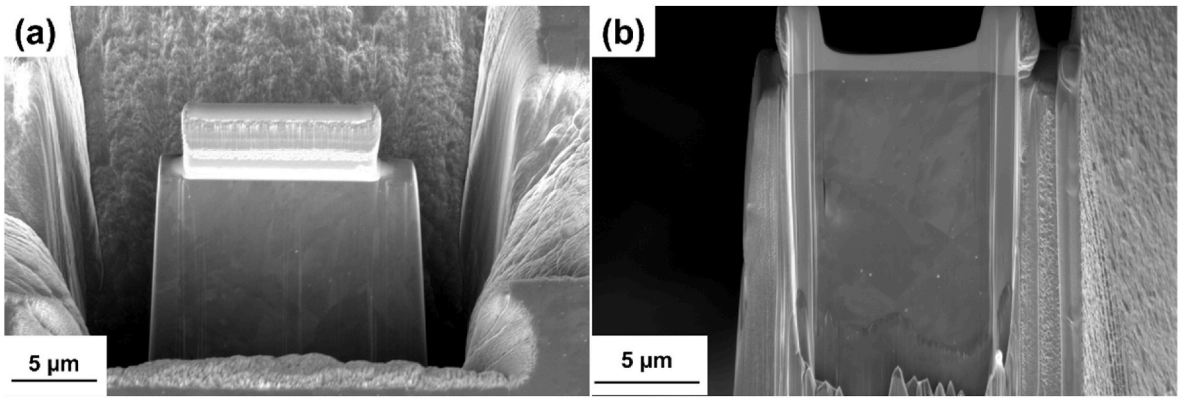

Fig. 2. (a) ion-milled trenches around the FIB sample and (b) thinned TEM lamella.

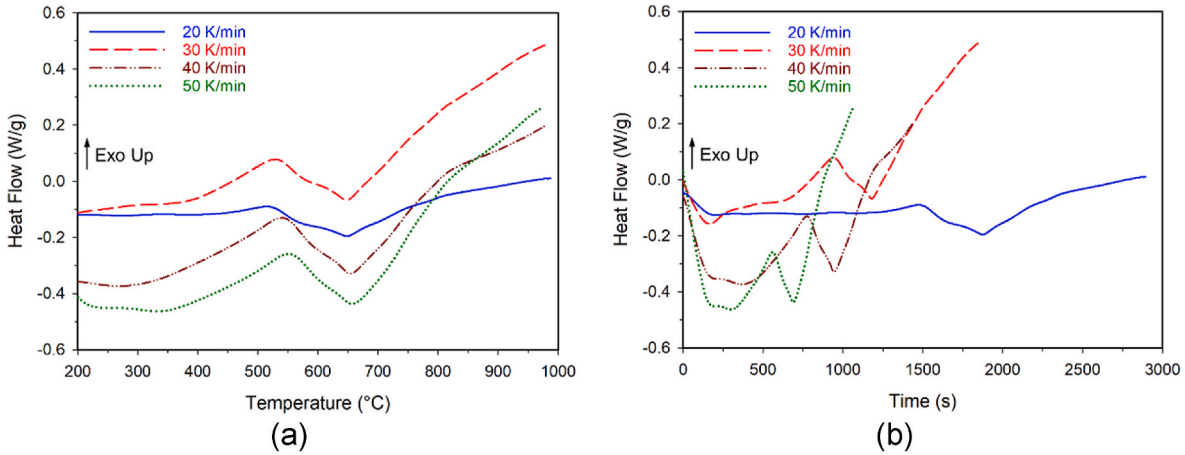

Fig. 3. DSC curves of L-PBF-CX with respect to (a) temperature and (b) time.

reverted austenite may form during the aging heat treatment. Therefore, it is essential to consider the kinetics of austenite reversion to count for it during designing the aging heat treatment for L-PBF-CX.

The analysis of the endothermic and exothermic peaks in the DSC curves requires the subtraction of the baseline [51]. The baseline represents the part of the curve that does not exhibit any transitions or reactions. Therefore, it should be subtracted from the DSC curve to obtain the actual heat flow associated with the phase transformation. The first step of the baseline subtraction is to determine the onset temperature (T_o) and end temperature (T_e) of the reaction. Since the baseline is temperature and time-dependent [52], the determination of T_o and T_e should be conducted for each heating rate separately. Once these characteristics are determined, the baseline is constructed considering the fact that T_o and T_e represents the start and end points of the baseline and then it is subtracted from the actual DSC curve [53]. T_o and T_e can be determined by taking the first derivative of the heat flow with respect to the temperature and identifying the points where the slope is changing abruptly, as shown in Fig. 4. After identifying T_o and T_e, the peak analyze module in the OriginPro 2021 software was employed for baseline subtraction [48]. Fig. 5 shows the processed peaks (after baseline subtraction) for the precipitation and austenite reversion phase transformations in the L-PBF-CX.

An important characteristic of the exothermic and endothermic peaks in any DSC analysis is the peak temperature, where the transformation reaches the maximum rate. Fig. 6 shows the effect of the heating rate on the peak temperatures of both transformations. By increasing the heating rate the peak temperature increases which is a common phenomenon in DSC studies [51]. The peak temperatures for precipitation and austenite reversion vary between 515-554 °C and 647–657 °C, respectively.

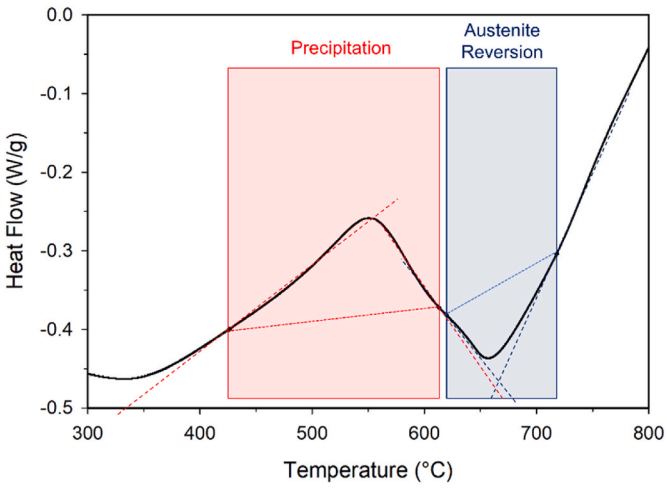

Fig. 4. Determination of onset and end temperatures of precipitation and austenite reversion peaks.

3.2. Degree of transformation and activation energy

The degree of phase transformation (transformed fraction, f) at any time/temperature can be determined by using the processed DSC curves (Fig. 5). The transformed fraction is equivalent to the fraction of heat

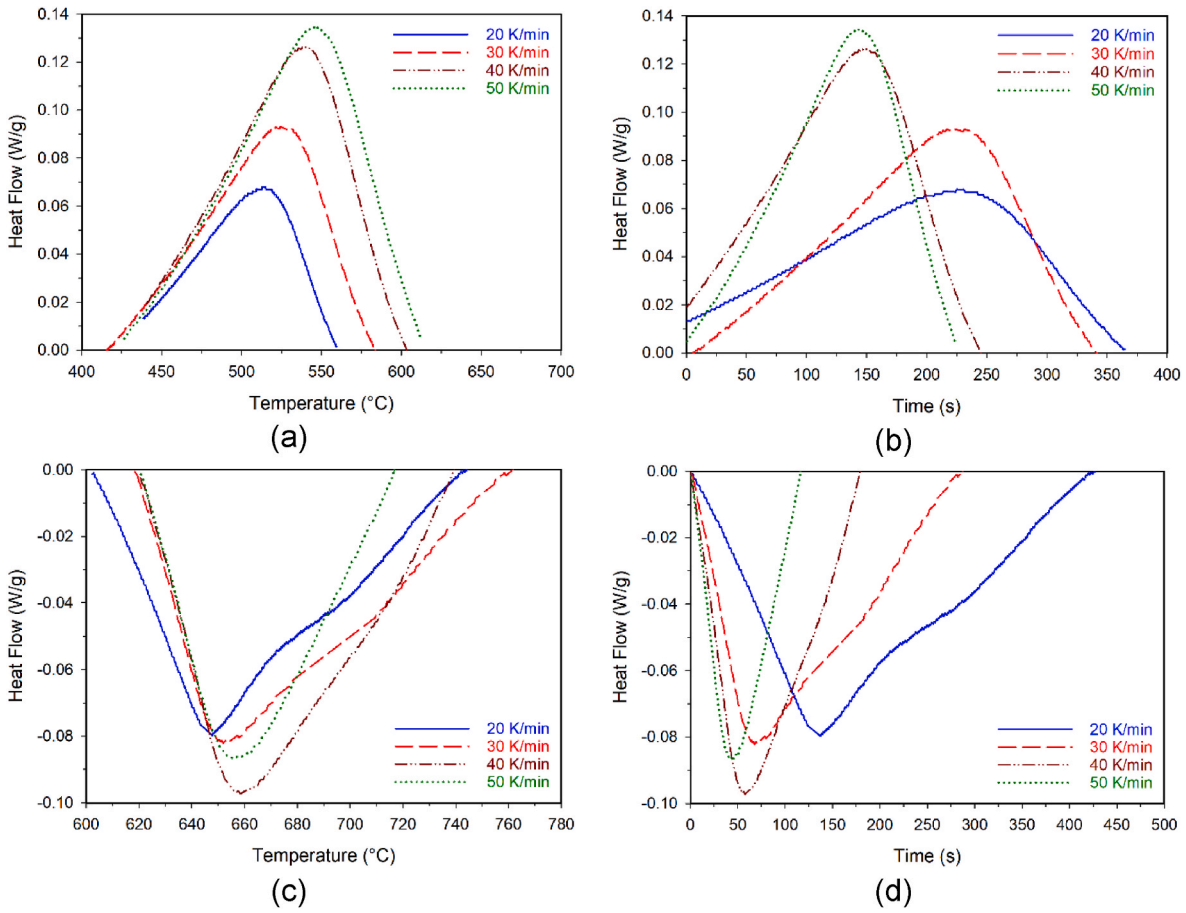

Fig. 5. Processed DSC peaks for precipitation with respect to (a) temperature and (b) time, and austenite reversion with respect to (c) temperature and (d) time.

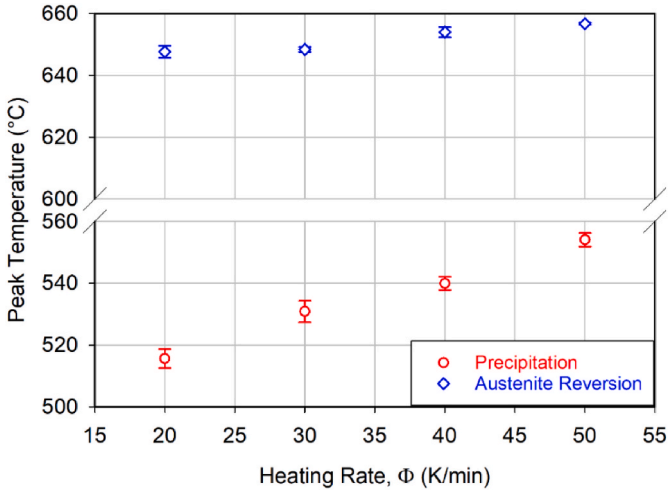

Fig. 6. The effect of heating rate on the peak temperatures of precipitation and austenite reversion.

that is absorbed/released during the transformation process and can be determined as follows [51],

$$f(t) = \frac{\int_{t_o}^{t} H dt}{\int_{t_o}^{t_e} H dt} \quad (1)$$

where $f(t)$ is the transformed fraction at any given time (t), H is the heat flow measured during the DSC, and t_o and t_e are the transformation onset and end times, respectively, associated with the onset and end temperatures. The denominator in Eq. (1) represents the total enthalpy of the transformation equivalent to the area under the processed peak curves in Fig. 5 (b) and (d). The results for both precipitation and austenite reversion transformations are plotted in Fig. 7. In both cases, the transformation follows the common sigmoidal trend. Moreover, by increasing the heating rate, the phase transformation is completed over a shorter period [51].

Determination of the kinetics model parameters begins with the

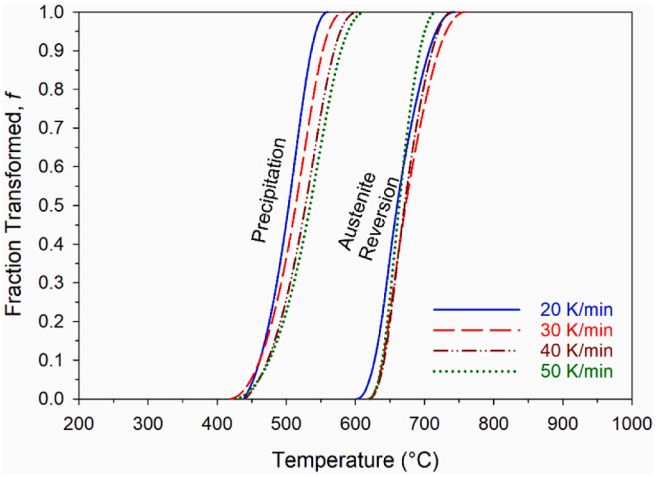

Fig. 7. Calculated degree of precipitation and austenite reversion using the DSC results at different heating rates.

evaluation of the transformation activation energy (E_a). E_a is a thermodynamics parameter that represents the minimum energy required for the initiation of the process. In the case of the availability of non-isothermal DSC results at different heating rates, E_a can be determined using the modified Kissinger method [48,51,54], as follows,

$$ln\frac{T_P^2}{\Phi}=\frac{E_a}{RT_P}+constant \tag{2}$$

where T_P is the process peak temperature (in K) (Fig. 6), Φ is the heating rate (in K/s), R is the universal gas constant (8.314 J/mol.K), and E_a is the activation energy in J/mol. Referring to Eq. (2), the activation energy can be determined by linear regression between $ln\frac{T_P^2}{\Phi}$ and $\frac{1000}{T_P}$ data as shown in Fig. 8. The slope of the line is equivalent to $\frac{E_a}{R}$, where the activation energy can be then determined. In the current study, the activation energy for precipitation and austenite reversion was evaluated as 118.6 kJ/mol and 591.1 kJ/mol, respectively. The activation energy for precipitation in a conventionally manufactured counterpart (*i.e.* investment cast PH 13-8 Mo stainless steel) was evaluated as 139 kJ/mol [55] which is higher than that of the L-PBF-CX. The main reason for such a difference is the higher dislocation density in the L-PBF alloys [21,43,56] compared to the conventionally manufactured ones. The high-density dislocations act as pipelines for the diffusion of the alloying elements [57] and facilitate the nucleation and growth processes [58]. As a result, the precipitation activation energy is lowered.

3.3. Non-isothermal and isothermal phase transformation kinetics parameters

The kinetics of phase transformations under non-isothermal heating conditions is usually studied by employing the modified Johnson-Mehl-Avrami-Kolmogorov (JMAK) model [51]. The common JMAK model has been widely used to investigate the isothermal phase transformations [59–62], as follows

$$f=1-\exp\left[-(kt)^n\right] \tag{3}$$

where f is the fraction transformed at time t, n is the Avrami constant, and k is the reaction rate. For the isothermal processes, k is independent of the temperature. However, in the modified JMAK model, a temperature-dependent reaction rate has been established as follows [63,64]

$$k(T)=k_0\exp\left(-\frac{E_a}{RT}\right) \tag{4}$$

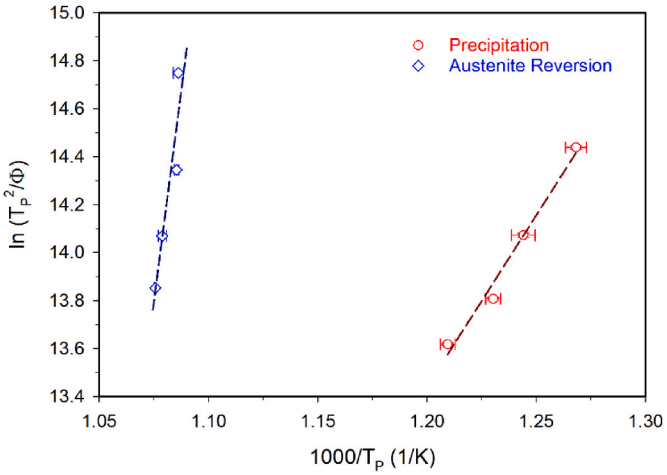

Fig. 8. Kissinger plot for precipitation and austenite reversion to determine the activation energy.

where $k(T)$ is the temperature-dependent reaction rate and k_0 is the pre-exponential factor. E_a should be determined using the Kissinger method (Eq. (2) and Fig. 8). Therefore, the general JMAK model can be derived as follows

$$f=1-\exp\left[-\left(\int_{t_o}^{t}k(T)dt\right)^n\right] \tag{5}$$

The general JMAK equation (Eq. (5)) is valid for a constant temperature, however, for continuous heating with a heating rate of $\Phi=\frac{dT}{dt}$, the JMAK equation is revised as follows [63,65,66]

$$f=1-\exp\left[-\left(\left(\frac{1}{\Phi}\right)\int_{T_o}^{T}k(T)dT\right)^n\right] \tag{6}$$

By implementing $k(T)$ from Eq. (4) into Eq. (6), the modified JMAK equation to model the non-isothermal phase transformation kinetics at any temperature T (in K) is derived as follows [67,68]

$$f=1-\exp\left[-\left(\frac{k_0}{\Phi}\left(exp\frac{-E_a}{RT}\right)(T-T_o)\right)^n\right] \tag{7}$$

where Φ is the heating rate (in K/s or °C/s) and T_o is the onset temperature of the phase transformation determined from the DSC curves. The values for k_0 and n were determined by curve fitting to the experimental transformed fraction plots (Fig. 7) obtained from the DSC for each heating rate, by employing the activation energy values evaluated using the Kissinger method. In the next step, an average was taken over the k_0 and n values to determine the corresponding parameters for the precipitation and austenite reversion processes [51]. The parameters were determined as $n=0.95$ and $k_0=2.85\times10^5$ for precipitation and $n=0.40$ and $k_0=3.28\times10^{30}$ for autenite reversion. These values can be then employed to model the kinetics of precipitation and austenite reversion during an isothermal aging process by using Eq. (3) [51]. To determine the value for the reaction rate (k) at the aging temperature, Eq. (4) could be employed.

3.4. Design of heat treatment

The results of the isothermal kinetics models were employed to age the as-built L-PBF-CX at different temperatures in the range of 400–600 °C to assess the model's efficiency. The hold time at each temperature was determined by employing the isothermal kinetics modeling results to achieve 100% precipitate fraction transformation. The aging conditions are summarized in Table 2.

The hardness of the samples was measured after the aging treatments and the results are shown in Fig. 9. As observed, the hardness of the as-built-CX was 34.9 ± 2.9 HRC, which is in agreement with those reported previously [32,69]. After aging the material at 400–600 °C, the hardness increased due to the formation of β-NiAl precipitates. The extreme aging temperatures, *i.e.* 400 °C and 600 °C did not result in the maximum hardness of the material. It appears that the precipitates that formed at 400 °C did not possess the characteristics of effective precipitates such as size and coherency, which requires further microstructural analyses. On the other hand, at 600 °C precipitate coarsening may have occurred [1] which resulted in hardness reduction. In addition, the formation of extensive reverted austenite at 600 °C (close to 17%, based on the kinetics models) could be another reason for hardness deterioration. The aging heat treatments at 460–550 °C resulted in hardness values in the range of 50–51 HRC, which is the common hardness of hardened L-PBF-CX [30–32,69]. Therefore, the isothermal kinetics modeling

Table 2
Aging conditions of L-PBF-CX.

Aging temperature (°C)	400	460	495	530	550	600
Aging time (min)	1667	1078	424	180	115	40

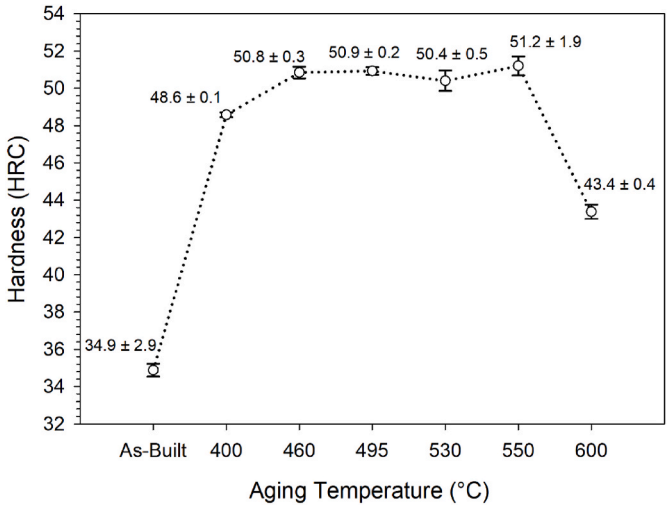

Fig. 9. Hardness of L-PBF-CX after aging heat treatment.

results could be successfully employed to determine the aging temperature and time for the L-PBF-CX. In addition, the L-PBF-CX could be aged over a range of temperatures (460–550 °C) rather than a single temperature (530 °C). Referring to the hardness results, it appears that the optimum aging condition is 550 °C/115 min rather than the common 530 °C/180 min, which resulted in the maximum hardness for the range of studied conditions.

3.5. Strength, ductility, and microstructure of heat-treated L-PBF-CX

By employing the optimum aging condition (*i.e.* 550 °C/115 min), the L-PBF-CX rods were directly aged. Fig. 10 shows the tensile properties of the as-built and heat-treated (directly aged) L-PBF-CX. As seen, the as-built material possesses yield and tensile strengths of 929 MPa and 1032 MPa, respectively with a total elongation of 15.3%. These properties are consistent with those reported previously by other researchers as listed in Table 1. After direct aging at 550 °C for 115 min, the yield and tensile strengths significantly improved to 1659 MPa and 1738 MPa, while the total elongation to fracture slightly reduced to 14.7%. Both strength enhancement and ductility retention are phenomenal for the heat-treated L-PBF-CX, as shown in Fig. 11. Referring to Fig. 11 (a), the strength of heat-treated L-PBF-CX in this study is the highest among the available values in the literature. On the other hand, while the heat treatment of L-PBF-CX generally results in a

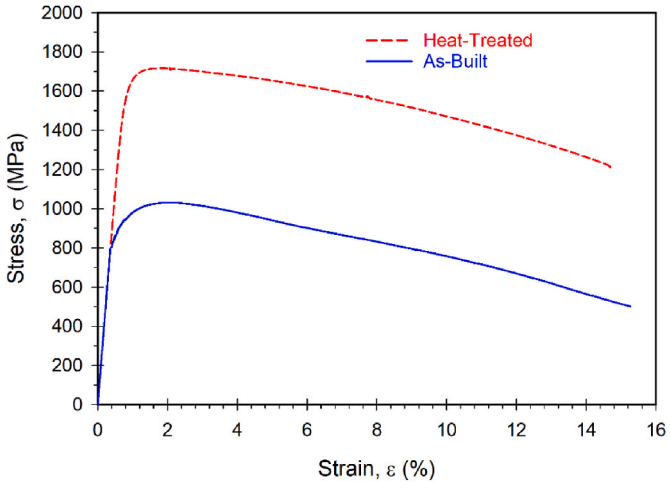

Fig. 10. Tensile properties of as-built and heat-treated L-PBF-CX.

reduction in ductility, as seen in Fig. 11 (b), the suggested heat treatment in our study did not deteriorate the ductility. In other words, the accurate aging of the L-PBF-CX maraging steel considering the kinetics of phase transformations resulted in the strength-ductility trade-off enhancement. It appears from the results that preserving the original microstructure developed during the L-PBF process is the governing mechanism in strength enhancement and ductility retention.

To further analyze the effect of direct aging, the microstructure of the heat-treated material was studied using TEM. Fig. 12 shows the TEM bright field (BF) of the heat-treated L-PBF-CX with details of the lath martensitic structure and the dislocation networks. The martensite laths are featured by the networks of entangled dislocations. These are the pre-existing dislocation networks, developed during the rapid solidification in the L-PBF process, and preserved during the low-temperature aging treatment. Apparently, this TEM micrograph does not reveal any evidence of β-NiAl formation. Due to the ultrafine size of β-NiAl precipitates which is < 10 nm [11] and the full coherency between these precipitates and the martensitic matrix [43], the lattice misfit strain is $<1\%$ [12]. Therefore, revealing them using TEM imaging is challenging. However, superlattice reflections are observed in the selected area diffraction (SAD) patterns due to the ordered structure of the β-NiAl precipitates [11,43].

With the beam aligned parallel to the $[001]_{Fe/\beta-NiAl}$ direction, an SAD pattern was obtained from one of the martensite laths as shown in Fig. 13 (a) and (b). The main diffraction spots associated with the martensitic matrix along with the weak superlattice spots associated with the β-NiAl precipitates are visible in the SAD pattern. The corresponding dark-field (DF) image taken from a superlattice reflection is shown in Fig. 13 (c). The DF image reveals the nano-scaled β-NiAl precipitates dispersed in the lath martensite. The evolution of the nanometric precipitates is the main reason for strength enhancement in the aged L-PBF-CX [43].

The microstructure of the heat-treated L-PBF-CX was also analyzed in the scanning mode of TEM (STEM), and the STEM-BF image along with the corresponding EDS (energy dispersive X-Ray spectroscopy) maps of Al and Ni are shown in Fig. 14. The STEM-BF image of the material does not exhibit any evidence of the existence of the β-NiAl precipitates, as observed in the TEM images as well. However, the EDS elemental maps exhibit a good distribution of the nanometric precipitates in the matrix. Referring to the STEM-BF image, more details of the pre-existing dislocation networks are observed. These networks are interconnected and distributed in the microstructure of the material. These dislocations evolved as a result of the rapid solidification of the melt pools during the L-PBF process [43]. The presence of the pre-existing dislocation networks has a crucial effect on the mechanical properties of L-PBF steels since they can effectively improve ductility [70] by increasing the dislocation storage capability [71]. In addition, the dislocation networks can effectively facilitate precipitation since they act as pipelines for the diffusion of the substitutional elements [57]. Therefore, preserving the dislocations during any post-processing heat treatment of L-PBF steels is critical to ensure their benefits on the physical and mechanical properties. The employment of a low-temperature aging treatment in the current study by avoiding the high-temperature austenitization step effectively preserved the dislocation networks that resulted in the enhancement of both strength and ductility.

4. Discussion

The low-temperature aging heat treatment of the L-PBF-CX had two crucial roles in breaking the strength-ductility trade-off; preserving the dislocation networks and evolution of the nano-scaled β-NiAl precipitates. The microstructure of L-PBF-CX in the as-built condition with the same geometry and process parameters has been reported by Sanjari et al. [42]. The TEM analysis of the as-built L-PBF-CX revealed the entangled pre-existing dislocation networks in the microstructure of the material. Meanwhile, no evidence of β-NiAl precipitates was observed.

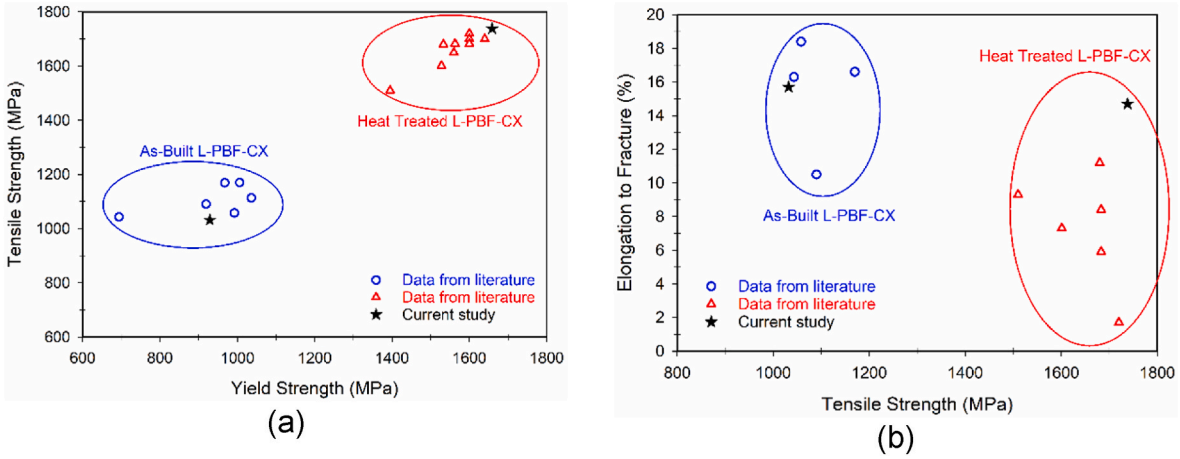

Fig. 11. Summary of strength and ductility of as-built and heat-treated L-PBF-CX, data from the literature are summarized in Table 1.

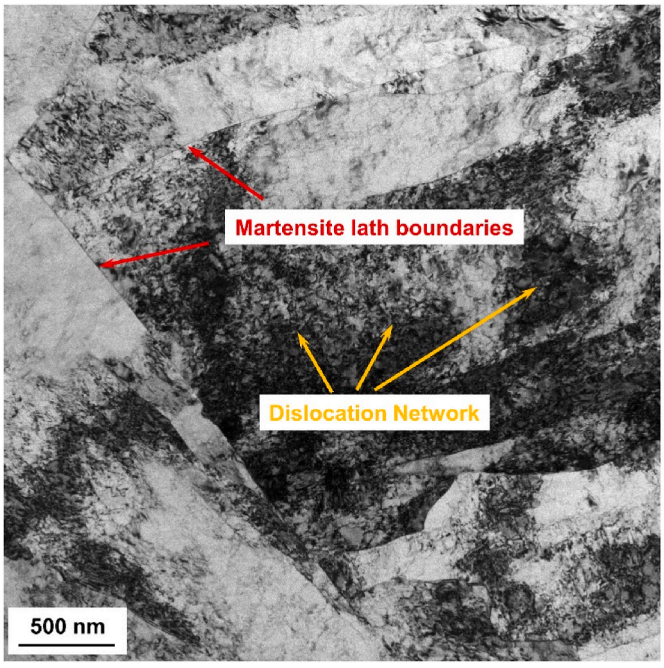

Fig. 12. TEM micrograph of heat-treated L-PBF-CX, showing the details of lath martensitic structure and the network of entangled dislocations.

The absence of the hardening precipitates in the as-fabricated (non-heat treated) maraging stainless steels is a common phenomenon reported by other researchers as well [11]. Therefore, the main strengthening mechanisms in the as-built L-PBF-CX are sub-boundary hardening (controlled by the martensite laths) and dislocation hardening (controlled by the pre-existing dislocation networks).

The TEM results reported by Sanjari et al. [42] for the as-built material and those reported in the current study for the heat-treated sample (Fig. 14) were employed to calculate the dislocation density. It should be noted that samples by Sanjari et al. [42] were fabricated using the same process parameters and geometry on the same printing machine as the current study. The dislocation density was determined by the method proposed by Pesicka et al. [72] and Rojas et al. [73]. The square grid lines were superimposed on the STEM micrographs and the number of horizontal (n_h) and vertical (n_v) dislocations-grid lines intersections were counted. The thickness of the TEM foild (t) was determined using electron-energy loss spectroscopy (EELS) log ratio technique [74], and the dislocation density was calculated as follows,

$$\rho_d = \frac{1}{t}\left(\frac{\sum n_v}{\sum L_v} + \frac{\sum n_h}{\sum L_h}\right) \tag{8}$$

where ρ_d is the dislocation density (in m^{-2}) and $\sum L_h$ and $\sum L_v$ are the total length of the horizontal and vertical lines, respectively. The values of the parameters used in Eq. (8) are shown in Table 3.

Using this method, the dislocation density in the as-built and heat-treated L-PBF-CX was estimated as 1.2×10^{15} m^{-2} and 1.08×10^{15} m^{-2}, respectively. As observed, the low-temperature aging preserved 90% of the pre-existing dislocations. Therefore, these dislocations can

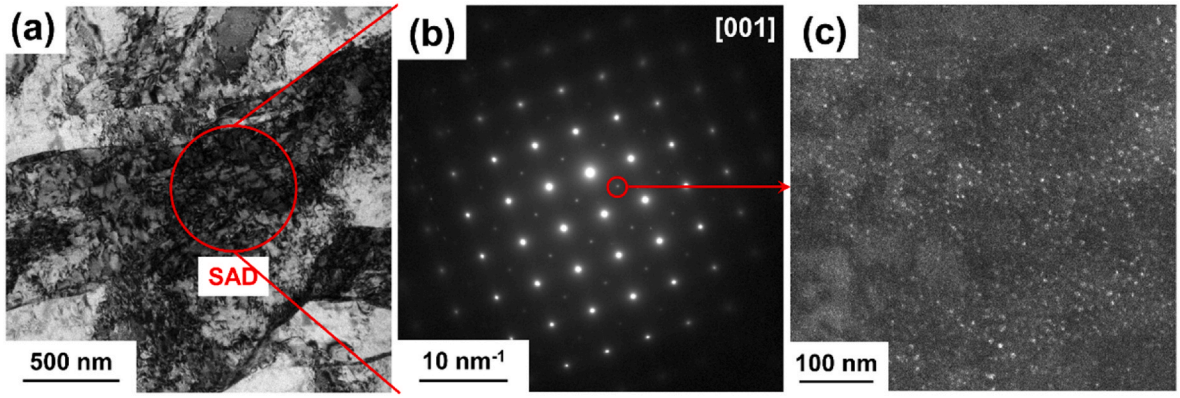

Fig. 13. (a) TEM-BF image of heat-treated L-PBF-CX, (b) SAD showing the main diffraction spots from the martensitic matrix and superlattice spots from β-NiAl nanoscaled precipitates, and (c) dark-field image of the matrix using the β-NiAl superlattice reflection.

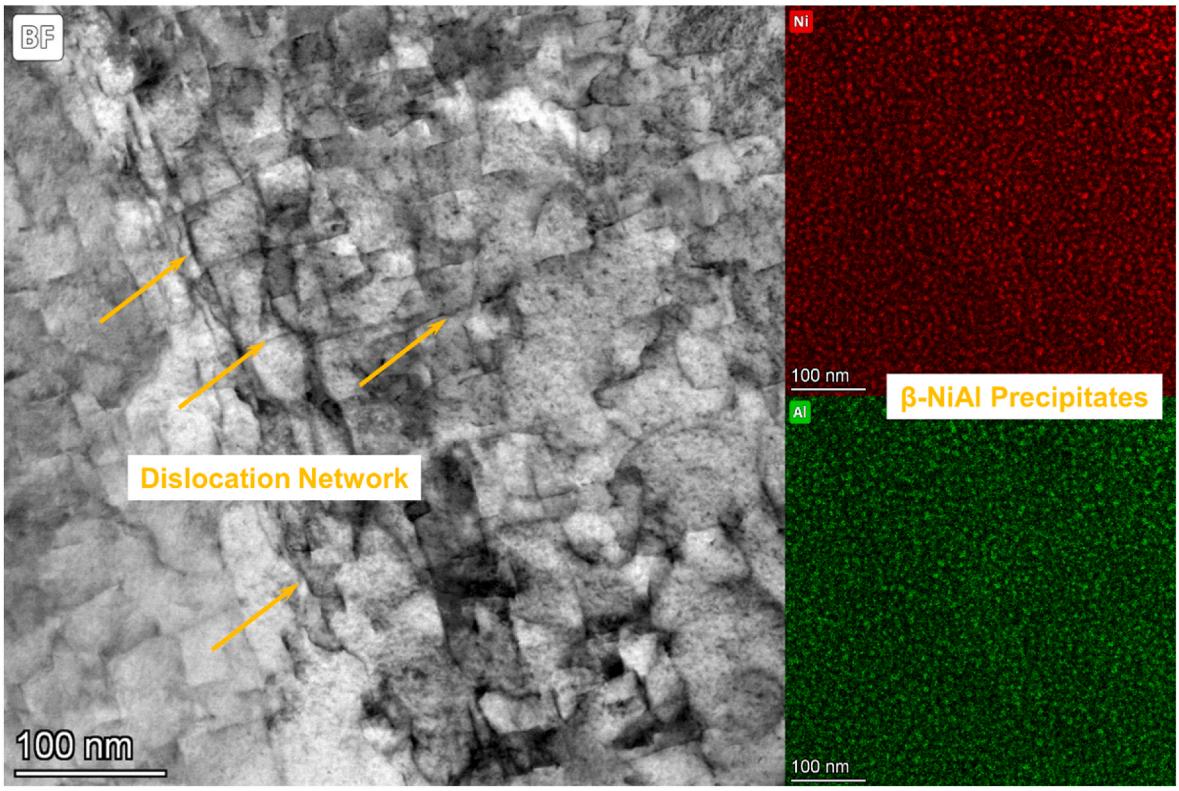

Fig. 14. Left: STEM-BF image of the heat-treated L-PBF-CX, right: corresponding EDS elemental maps of Ni and Al.

Table 3
Quantities used in Eq. (8).

	Σn_v	ΣL_v (nm)	Σn_h	ΣL_h (nm)	t (nm)	ρ_d (m^{-2})
As-built	39	1727	65	1727	50	1.2×10^{15}
Heat-treated	34	804	27	804	70	1.08×10^{15}

effectively contribute to both strength and ductility. The survey of the mechanical properties obtained in the current study and those available in the literature (Fig. 11) reveals a significant difference in the ductility of the heat-treated L-PBF-CX. We believe that the preserved dislocations are the main reason for ductility retention. Liu et al. [70] showed that the pre-existing dislocation networks in the L-PBF steels maintain their configuration during the plastic deformation and act as an ideal "modulator" to slow down the dislocation motion. The in-situ TEM study by Liu et al. [70] showed that these networks significantly, and not fully, impede the dislocation motion during the plastic deformation. Therefore, these networks increase the dislocation storage capacity of the material which results in ductile plastic deformation. The preserved pre-existing dislocation networks in the current study are playing the same role; they maintain the dislocation storage capacity of aged L-PBF-CX during the plastic deformation and retain ductility.

Using the TEM-EDS elemental maps (Fig. 14) the average size, volume fraction, and inter-particle distance of β-NiAl precipitates were estimated as 8.8 nm, 3.4%, and 13.9 nm, respectively. The strength increment due to the evolution of nano-scaled β-NiAl precipitates ($\Delta\sigma_p$) is governed by three factors [43,75]: order strengthening ($\Delta\sigma_o$), coherency strengthening ($\Delta\sigma_c$), and modulus mismatch strengthening ($\Delta\sigma_m$), as follows,

$$\Delta\sigma_p = \Delta\sigma_o + \Delta\sigma_c + \Delta\sigma_m = 0.4M\frac{\gamma_{APB}}{b}\left(\frac{3\pi f}{8}\right)^{1/2} + 2.6M(\varepsilon G)^{3/2}\left(\frac{2rf}{Gb}\right)^{1/2} + 0.0055M(\Delta G)^{\frac{3}{2}}\left(\frac{2f}{Gb^2}\right)^{\frac{1}{2}} b\left(\frac{r}{b}\right)^{\frac{3m}{2}-1} \quad (9)$$

where M is the Taylor factor, γ_{APB} is the anti-phase boundary (APB) energy of the β-NiAl, b is the Burgers vector, f is the volume fraction of β-NiAl, G is the shear modulus of the matrix, r is the mean radius of β-NiAl, ε is the lattice mismatch parameter, ΔG is the shear modulus mismatch between β-NiAl and matrix, and m is a constant. Table 4 summarizes the parameters used in determining the β-NiAl precipitation strength increment. The modeled strength increment in the aged L-PBF-CX due to the evolution of nano-scaled β-NiAl precipitates was estimated as $\Delta\sigma_p = 779$ MPa. Referring to the tensile properties reported in Fig. 10 and Fig. 11, the experimental strength increment ($\Delta\sigma_y$) after heat treatment was 730 MPa. The marginal discrepancy between the modeled and experimental values stems from two main reasons: (1) strength reduction due to the annihilation of 10% of the dislocations during the heat treatment which compensates for a portion of such a difference and (2) the nature of a modeling approach where some simplifying assumptions are made. Nevertheless, the precipitates are playing a significant role in strength enhancement in the heat-treated L-PBF-CX.

Table 4
Parameters used in Eq. (9).

Parameter	Unit	Value	Reference
M	–	2.9	[11]
γ_{APB}	mJ m^{-2}	500	[11]
b	nm	0.25	[43]
f	–	0.034	Current study
ε	–	0.0064	[43]
G	GPa	77	[11]
r	nm	4.4	Current study
ΔG	GPa	4	[11]
m	–	0.85	[11]

5. Conclusions

In the current study, differential scanning calorimetry (DSC) was employed to determine the heat flow curves in a laser-powder bed fused (L-PBF) CX maraging steel (belonging to the PH 13-8 Mo family). The DSC runs were conducted at different heating rates of 20–50 °C/min to a maximum temperature of 1000 °C. The DSC curves were then analyzed to identify the peaks associated with precipitation and austenite reversion phase transformations. The former process exhibited an exothermic peak while the latter exhibited an endothermic peak. The peaks were processed to subtract the baseline and in the next step the onset, peak, and end temperatures of each phase transformation as a function of heating rate were determined. The heat flow associated with each processed peak was used to determine the degree of phase transformation during precipitation and austenite reversion. The peak temperatures were used to determine the activation energy of the phase transformation using the Kissinger method. The activation energy for precipitation and austenite reversion was evaluated as 118.6 kJ/mol and 591.1 kJ/mol, respectively. The activation energy for precipitation in L-PBF-CX was lower than that of a conventionally manufactured counterpart (139 kJ/mol). The main reason for such a difference is the higher dislocation density in the L-PBF-CX. In the next step, the modified Johnson-Mehl-Avrami-Kolmogorov (JMAK) model was employed to model the kinetics of phase transformations during non-isothermal heating. The good agreement between the experimental and modeled degree of transformation confirmed the suitability and effectiveness of the JMAK model. Therefore, this model was employed to predict the degree of precipitation and austenite reversion during isothermal aging at 400–550 °C. The material was aged over this range of temperatures and the hardness was measured. It was observed that the optimum aging condition is 550 °C/115 min rather than the common 530 °C/180 min, which resulted in the maximum hardness for the range of studied conditions. The tensile properties of the heat-treated L-PBF-CX at 550 °C/115 min were evaluated. It was observed that direct aging of L-PBF-CX enhanced the yield strength from 929 MPa to 1659 MPa and the tensile strength from 1032 MPa to 1738 MPa. Meanwhile, the elongation to fracture slightly decreased from 15.3% in the as-built condition to 14.7% after heat treatment. Such a phenomenal achievement in breaking the strength-ductility trade-off in the L-PBF-CX maraging steel was due to the evolution of nanometric β-NiAl precipitates while the entangled dislocation networks were preserved during the low-temperature heat treatment. The precipitates enhanced the strength and the dislocations retained the ductility.

CRediT authorship contribution statement

Richard Fabian: Methodology, Validation, Investigation, Writing – original draft. **Amir Hadadzadeh:** Conceptualization, Methodology, Validation, Investigation, Resources, Writing – review & editing, Supervision.

Declaration of competing interest

The authors declare that they have no known competing financial interests or personal relationships that could have appeared to influence the work reported in this paper.

Data availability

The data that has been used is confidential.

Acknowledgments

The authors would like to acknowledge the Herff College of Engineering at the University of Memphis for the financial support of the research through the HCOE-FRG program. The authors acknowledge Mr. Moniruzzaman for helping in heat treating the samples and hardness measurements and Dr. Molaei for conducting the tensile tests.

References

[1] Z. Guo, W. Sha, D. Vaumousse, Microstructural evolution in a PH13-8 stainless steel after ageing, Acta Mater. 51 (2003) 101–116, https://doi.org/10.1016/S1359-6454(02)00353-1.
[2] E.A. Jägle, Z. Sheng, P. Kürnsteiner, S. Ocylok, A. Weisheit, D. Raabe, Comparison of maraging steel micro- and nanostructure produced conventionally and by laser additive manufacturing, Materials 10 (2017) 8, https://doi.org/10.3390/ma10010008.
[3] L. Zai, C. Zhang, Y. Wang, W. Guo, D. Wellmann, X. Tong, Y. Tian, Laser powder bed fusion of precipitation-hardened martensitic stainless steels: a review, Metals 10 (2020) 255, https://doi.org/10.3390/met10020255.
[4] B. Pollard, Selection of wrought precipitation-hardening stainless steels, in: ASM Handbook, 6, ASM, Materials Park, OH, 1993, pp. 482–494.
[5] R. Schnitzer, R. Radis, M. Nöhrer, M. Schober, R. Hochfellner, S. Zinner, E. Povoden-Karadeniz, E. Kozeschnik, H. Leitner, Reverted austenite in PH 13-8 Mo maraging steels, Mater. Chem. Phys. 122 (2010) 138–145, https://doi.org/10.1016/j.matchemphys.2010.02.058.
[6] P. Liu, A.H. Stigenberg, J.O. Nilsson, Quasicrystalline and crystalline precipitation during isothermal tempering in a 12Cr-9Ni-4Mo maraging stainless steel, Acta Metall. Mater. 43 (7) (1995) 2881–2890, https://doi.org/10.1016/0956-7151(94)00461-.
[7] H.J. Kong, C.T. Liu, A review on nano-scale precipitation in steels, Technologies 6 (2018) 36, https://doi.org/10.3390/technologies6010036.
[8] S.D. Erlach, H. Leitner, M. Bischof, H. Clemens, F. Danoix, D. Lemarchand, I. Siller, Comparison of NiAl precipitation in a medium carbon secondary hardening steel and C-free PH13-8 maraging steel, Mater. Sci. Eng., A 429 (2006) 96–106, https://doi.org/10.1016/j.msea.2006.05.071.
[9] Z.B. Jiao, J.H. Luan, Z.W. Zhang, M.K. Miller, C.T. Liu, High-strength steels hardened mainly by nanoscale NiAl precipitates, Scripta Mater. 87 (2014) 45–48, https://doi.org/10.1016/j.scriptamat.2014.05.006.
[10] D.H. Ping, M. Ohnuma, Y. Hirakawa, Y. Kadoya, K. Hono, Microstructural evolution in 13Cr–8Ni–2.5Mo–2Al martensitic precipitation-hardened stainless steel, Mater. Sci. Eng., A 394 (2005) 285–295, https://doi.org/10.1016/j.msea.2004.12.002.
[11] L. Sun, T.H. Simm, T.L. Martin, S. McAdam, D.R. Galvin, K.M. Perkins, P.A. J. Bagot, M.P. Moody, S.W. Ooi, P. Hill, M.J. Rawson, H.K.D.H. Bhadeshia, A novel ultra-high strength maraging steel with balanced ductility and creep resistance achieved by nanoscale β-NiAl and Laves phase precipitates, Acta Mater. 149 (2018) 285–301, https://doi.org/10.1016/j.actamat.2018.02.044.
[12] Z.K. Teng, G. Ghosh, M.K. Miller, S. Huang, B. Clausen, D.W. Brown, P.K. Liaw, Neutron-diffraction study and modeling of the lattice parameters of a NiAl-precipitate-strengthened Fe-based alloy, Acta Mater. 60 (2012) 5362–5369, https://doi.org/10.1016/j.actamat.2012.05.033.
[13] S. Jiang, H. Wang, Y. Wu, X. Liu, H. Chen, M. Yao, B. Gault, D. Ponge, D. Raabe, A. Hirata, M. Chen, Y. Wang, Z. Lu, Ultrastrong steel via minimal lattice misfit and high-density nanoprecipitation, Nature 544 (2017) 460–464, https://doi.org/10.1038/nature22032.
[14] T. DebRoy, H.L. Wei, J.S. Zuback, T. Mukherjee, J.W. Elmer, J.O. Milewski, A. M. Beese, A. Wilson-Heid, A. De, W. Zhang, Additive manufacturing of metallic components – process, structure and properties, Prog. Mater. Sci. 92 (2018) 112–224, https://doi.org/10.1016/j.pmatsci.2017.10.001.
[15] D. Herzog, V. Seyda, E. Wycisk, C. Emmelmann, Additive manufacturing of metals, Acta Mater. 117 (2016) 371–392, https://doi.org/10.1016/j.actamat.2016.07.019.
[16] W.J. Sames, F.A. List, S. Pannala, R.R. Dehoff, S.S. Babu, The metallurgy and processing science of metal additive manufacturing, Int. Mater. Rev. 61 (2016) 315–360, https://doi.org/10.1080/09506608.2015.1116649.
[17] Standard terminology for additive manufacturing – general principles – terminology, ASTM Int 52900 (2015) 2015 (E).
[18] D.D. Gu, W. Meiners, K. Wissenbach, R. Poprawe, Laser additive manufacturing of metallic components: materials, processes and mechanisms, Int. Mater. Rev. 57 (2012) 133–164, https://doi.org/10.1179/1743280411Y.0000000014.
[19] J.H. Martin, B.D. Yahata, J.M. Hundley, J.A. Mayer, T.A. Schaedler, T.M. Pollock, 3D printing of highstrength aluminium alloys, Nature 549 (2017) 365–369, https://doi.org/10.1038/nature23894.
[20] B.H. Jared, M.A. Aguilo, L.L. Beghini, B.L. Boyce, B.W. Clark, A. Cook, B.J. Kaehr, J. Robbins, Additive manufacturing: toward holistic design, Scripta Mater. 135 (2017) 141–147, https://doi.org/10.1016/j.scriptamat.2017.02.029.
[21] Y.M. Wang, T. Voisin, J.T. McKeown, J. Ye, N.P. Calta, Z. Li, Z. Zeng, Y. Zhang, W. Chen, T.T. Roehling, R.T. Ott, M.K. Santala, P.J. Depond, M.J. Matthews, A. V. Hamza, T. Zhu, Additively manufactured hierarchical stainless steels with high strength and ductility, Nat. Mater. 17 (2018) 63–70, https://doi.org/10.1038/NMAT5021.
[22] L. Thijs, K. Kempen, J.P. Kruth, J.V. Humbeeck, Fine-structured aluminium products with controllable texture by selective laser melting of pre-alloyed AlSi10Mg powder, Acta Mater. 61 (2013) 1809–1819, https://doi.org/10.1016/j.actamat.2012.11.052.
[23] EOS, GmbH—Electro Optical Systems, Material Data Sheet: EOS Stainless Steel CX, München, 2022. www.eos.info.
[24] H. Asgari, M. Mohammadi, Microstructure and mechanical properties of stainless steel CX manufactured by Direct Metal Laser Sintering, Mater. Sci. Eng., A 709 (2018) 82–89, https://doi.org/10.1016/j.msea.2017.10.045.

[25] Q. Saby, J.Y. Buffiere, E. Maire, T. Joffre, J. Bajolet, S. Garabedian, P. Vikner, X. Boulnat, Laser Powder Bed Fusion printability of cobalt-free steel powders for manufacturing injection molds, Addit. Manuf. 44 (2021), 102031, https://doi.org/10.1016/j.addma.2021.102031.
[26] M. Sanjari, A. Hadadzadeh, H. Pirgazi, A. Shahriari, B.S. Amirkhiz, L.A.I. Kestens, M. Mohammadi, Selective laser melted stainless steel CX: role of built orientation on microstructure and micro-mechanical properties, Mater. Sci. Eng., A 786 (2020), 139365, https://doi.org/10.1016/j.msea.2020.139365.
[27] A. Shahriari, L. Khaksar, A. Nasiri, A. Hadadzadeh, B. Shalchi Amirkhiz, M. Mohammadi, Microstructure and corrosion behavior of a novel additively manufactured maraging stainless steel, Electrochim. Acta 339 (2020), 135925, https://doi.org/10.1016/j.electacta.2020.135925.
[28] H. Pirgazi, M. Sanjari, S. Tamimi, B.S. Amirkhiz, L.A.I. Kestens, M. Mohammadi, Texture evolution in selective laser melted maraging stainless steel CX with martensitic transformation, J. Mater. Sci. 56 (2021) 844–853, https://doi.org/10.1007/s10853-020-05290-2.
[29] T.M. Thorburn, Maraging Steel Fatigue Properties Processed by Forging and Additive Manufacturing, in: Master's Thesis, Chalmers University of Technology, Gothenburg, Sweden, 2019.
[30] N. Asnafi, J. Rajalampi, D. Aspenberg, A. Alveflo, Production tools made by additive manufacturing through laser-based powder bed fusion, Berg Huettenmaenn Monatsh 165 (2020) 125–136, https://doi.org/10.1007/s00501-020-00961-8.
[31] J. Minguella-Canela, S. Morales Planas, M.A. De los Santos-López, SLM manufacturing redesign of cooling inserts for high production steel moulds and benchmarking with other industrial additive manufacturing strategies, Materials 13 (2020) 4843, https://doi.org/10.3390/ma13214843.
[32] J. Zhang, M. Wang, L. Niu, J. Liu, J. Wang, Y. Liu, Z. Shi, Effect of process parameters and heat treatment on the properties of stainless steel CX fabricated by selective laser melting, J. Alloys Compd. 877 (2021), 160062, https://doi.org/10.1016/j.jallcom.2021.160062.
[33] C. Chang, X. Yan, R. Bolot, J. Gardan, S. Gao, M. Liu, H. Liao, M. Chemkhi, S. Deng, Influence of post-heat treatments on the mechanical properties of CX stainless steel fabricated by selective laser melting, J. Mater. Sci. 55 (2020) 8303–8316, https://doi.org/10.1007/s10853-020-04566-x.
[34] X. Yan, C. Chen, C. Chang, D. Dong, R. Zhao, R. Jenkins, J. Wang, Z. Ren, M. Liu, H. Liao, R. Lupoi, S. Yin, Study of the microstructure and mechanical performance of C-X stainless steel processed by selective laser melting (SLM), Mater. Sci. Eng., A 781 (2020), 139227, https://doi.org/10.1016/j.msea.2020.139227.
[35] D. Dong, C. Chang, H. Wang, X. Yan, W. Ma, M. Liu, S. Deng, J. Gardan, R. Bolot, H. Liao, Selective laser melting (SLM) of CX stainless steel: theoretical calculation, process optimization and strengthening mechanism, J. Mater. Sci. Technol. 73 (2021) 151–164, https://doi.org/10.1016/j.jmst.2020.09.031.
[36] C. Cheng, X. Yan, Z. Deng, Q. Chu, S. Deng, R. Bolot, M. Chemkhi, M. Liu, H. Liao, J. Gardan, Effect of heat treatment on residual stress and wear resistance of CX stainless steel manufactured by Selective Laser Melting, Procedia CIRP 104 (2021) 738–743, https://doi.org/10.1016/j.procir.2021.11.124.
[37] C. Chang, X. Yan, Z. Deng, B. Lu, R. Bolot, J. Gardan, S. Deng, M. Chemkhi, M. Liu, H. Liao, Heat treatment induced microstructural evolution, oxidation behavior and tribological properties of Fe-12Cr-9Ni-2Al steel (CX steel) prepared using selective laser melting, Surf. Coat. Technol. 429 (2022), 127982.
[38] S. Afkhami, V. Javaheri, E. Dabiri, H. Piili, T. Bjork, Effects of manufacturing parameters, heat treatment, and machining on the physical and mechanical properties of 13Cr10Ni1.7Mo2Al0.4Mn0.4Si steel processed by laser powder bed fusion, Mater. Sci. Eng., A 832 (2022), 142402, https://doi.org/10.1016/j.msea.2021.142402.
[39] S. Afkhami, V. Javaheri, E. Dabiri, H. Piili, T. Bjork, Data related to the microstructural identification and analyzing the mechanical properties of maraging stainless steel 13Cr10Ni1.7Mo2Al0.4Mn0.4Si (commercially known as CX) processed by laser powder bed fusion method, Data Brief 41 (2022), 107856.
[40] S. Afkhami, V. Javaher, K. Lipiainen, M. Amraei, E. Dabiri, T. Bjork, Fatigue performance of stainless tool steel CX processed by laser powder bed fusion, Mater. Sci. Eng., A 841 (2022), 143031, https://doi.org/10.1016/j.msea.2022.143031.
[41] A. Hadadzadeh, B. Shalchi Amirkhiz, J. Li, M. Mohammadi, Columnar to equiaxed transition during direct metal laser sintering of AlSi10Mg alloy: effect of building direction, Addit. Manuf. 23 (2018) 121–131, https://doi.org/10.1016/j.addma.2018.08.001.
[42] M. Sanjari, M. Mahmoudiniya, H. Pirgazi, S. Tamimi, M.H. Ghoncheh, A. Shahriairi, A. Hadadzadeh, B.S. Amirkhiz, M. Purdy, E.G. de Araujo, L. Kestens, M. Mohammadi, Microstructure, texture, and anisotropic mechanical behavior of selective laser melted maraging stainless steels, Mater. Char. 192 (2022), 112185, https://doi.org/10.1016/j.matchar.2022.112185.
[43] A. Hadadzadeh, A. Shahriari, B.S. Amirkhiz, J. Li, M. Mohammadi, Additive manufacturing of an Fe-Cr-Ni-Al maraging stainless steel: microstructure evolution, heat treatment, and strengthening mechanisms, Mater. Sci. Eng., A 787 (2020), 139470, https://doi.org/10.1016/j.msea.2020.139470.
[44] A. Shahriari, M. Sanjari, H. Pirgazi, F. Fazeli, B.S. Amirkhiz, L.A.I. Kestens, M. Mohammadi, Microstructural evolution in additively manufacture Fe-Cr-Ni maraging stainless steel, Metall. Mater. Trans. A 53 (2022) 1771–1792, https://doi.org/10.1007/s11661-022-06633-1.
[45] S. Primig, H. Leitner, Transformation from continuous-to-isothermal aging applied on a maraging steel, Mater. Sci. Eng., A 527 (2010) 4399–4405, https://doi.org/10.1016/j.msea.2010.03.084.
[46] R. Casati, J.N. Lemke, A. Tuissi, M. Vedani, Aging behaviour and mechanical performance of 18-Ni 300 steel processed by selective laser melting, Metals 6 (2016) 218, https://doi.org/10.3390/met6090218.
[47] C. Tan, K. Zhou, M. Kuang, W. Ma, T. Kuang, Microstructural characterization and properties of selective laser melted maraging steel with different build directions, Sci. Technol. Adv. Mater. 19 (2018) 746–758, https://doi.org/10.1080/14686996.2018.1527645.
[48] H.C. Kaushik, M. Habibnejad Korayem, A. Hadadzadeh, Determination of α to β phase transformation kinetics in laser-powder bed fused Ti–6Al–2Sn–4Zr–2Mo-0.08Si and Ti–6Al–4V alloys, Mater. Sci. Eng., A 860 (2022), 144294, https://doi.org/10.1016/j.msea.2022.144294.
[49] B. Fotovvati, S.A. Etesami, E. Asadi, Process-property-geometry correlations for additively-manufactured Ti-6Al-4V sheets, Mater. Sci. Eng., A 760 (2019) 431–447, https://doi.org/10.1016/j.msea.2019.06.020.
[50] A. Hadadzadeh, B.S. Amirkhiz, B. Langelier, J. Li, M. Mohammadi, Microstructural consistency in the additive manufactured metallic materials: a study on the laser powder bed fusion of AlSi10Mg, Addit. Manuf. 46 (2021), 102166, https://doi.org/10.1016/j.addma.2021.102166.
[51] Z. Guo, W. Sha, D. Li, Quantification of phase transformation kinetics of 18 wt.% Ni C250 maraging steel, Mater. Sci. Eng., A 373 (2004) 10–20, https://doi.org/10.1016/j.msea.2004.01.040.
[52] M.J. Starink, A. Dion, DSC study of precipitation in an Al–Mg–Mn alloy microalloyed with Cu, Thermochim. Acta 417 (2004) 5–11, https://doi.org/10.1016/j.tca.2004.01.013.
[53] ASTM E3174-21, Standard Practice for Determination of Kinetic Reaction Model Using Differential Scanning Calorimetry, 2021.
[54] H.E. Kissinger, Reaction kinetics in differential thermal analysis, Anal. Chem. 29 (1957) 1702–1706, https://doi.org/10.1021/ac60131a045.
[55] C.V. Robino, P.W. Hochanadel, G.R. Edwards, M.J. Cieslak, Heat treatment of investment cast PH 13-8 Mo stainless steel: Part II. Isothermal aging kinetics, Metall. Mater. Trans. A 25 (1994) 697–704, https://doi.org/10.1007/BF02665446.
[56] Q. Ding, Y. Zhong, J. Zou, J. Wu, Y.L. Chiu, J. Li, Z. Zhang, Q. Yu, Z. Shen, Dislocation network in additive manufactured steel breaks strength–ductility tradeoff, Mater. Today 21 (2018) 354–361, https://doi.org/10.1016/j.mattod.2017.11.004.
[57] R.H. Doremus, The role of dislocations in carbide precipitation in α-iron, Acta Metall. 6 (1958) 674–679, https://doi.org/10.1016/0001-6160(58)90058-0.
[58] U.K. Viswanathan, S. Banerjee, R. Krishnan, Effects of aging on the microstructure of 17-4 PH stainless steel, Mater. Sci. Eng., A 100 (1988) 181–189, https://doi.org/10.1016/0025-5416(88)90420-X.
[59] M. Avrami, Kinetics of phase change. I: general theory, J. Chem. Phys. 7 (1939) 1103–1112, https://doi.org/10.1063/1.1750380.
[60] M. Avrami, Kinetics of phase change. II Transformation-time relations for random distribution of nuclei, J. Chem. Phys. 8 (1940) 212–224, https://doi.org/10.1063/1.1750631.
[61] M. Avrami, Granulation, phase change, and microstructure kinetics of phase change. III, J. Chem. Phys. 9 (1941) 177–184, https://doi.org/10.1063/1.1750872.
[62] A.N. Kolmogorov, On the statistical theory of crystallization of metals [in Russian], Izv. Akad. Nauk SSSR, Ser. Mat. 3 (1937) 355–359.
[63] H. Li, K. Gai, L. He, C. Zhang, H. Cui, M. Li, Non-isothermal phase-transformation kinetics model for evaluating the austenization of 55CrMo steel based on Johnson-Mehl-Avrami equation, Mater. Des. 92 (2016) 731–741, https://doi.org/10.1016/j.matdes.2015.12.110.
[64] M. Rafiei, H. Mirzadeh, M. Malekan, Precipitation kinetics of γ" phase and its mechanism in a Nb-bearing nickel-based superalloy during aging, Vacuum 178 (2020), 109456, https://doi.org/10.1016/j.vacuum.2020.109456.
[65] J. Torrens-Serra, S. Venkataraman, M. Stoica, U. Kuehn, S. Roth, J. Eckert, Non-isothermal kinetic analysis of the crystallization of metallic glasses using the master curve method, Materials 4 (2011) 2231–2243, https://doi.org/10.3390/ma4122231.
[66] J.S. Blázquez, C.F. Conde, A. Conde, Non-isothermal approach to isokinetic crystallization processes: application to the nanocrystallization of HITPERM alloys, Acta Mater. 53 (2005) 2305–2311, https://doi.org/10.1016/j.actamat.2005.01.037.
[67] T. Paul, A. Loganathan, A. Agarwal, S.P. Harimkar, Kinetics of isochronal crystallization in a Fe-based amorphous alloy, J. Alloys Compd. 753 (2018) 679–687, https://doi.org/10.1016/j.jallcom.2018.04.133.
[68] Y.H. Li, C. Yang, L.M. Kang, H.D. Zhao, S.G. Qu, X.Q. Li, W.W. Zhang, Y.Y. Li, Non-isothermal and isothermal crystallization kinetics and their effect on microstructure of sintered and crystallized TiNbZrTaSi bulk alloys, J. Non-Cryst. Solids 432 (2016) 440–452, https://doi.org/10.1016/j.jnoncrysol.2015.11.005.
[69] J. Samei, H. Asgari, C. Pelligra, M. Sanjari, S. Salavati, A. Shahriari, M. Amirmaleki, M. Jahanbakht, A. Hadadzadeh, B. Shalchi Amirkhiz, M. Mohammadi, A hybrid additively manufactured martensitic-maraging stainless steel with superior strength and corrosion resistance for plastic injection molding dies, Addit. Manuf. 45 (2021), 102068, https://doi.org/10.1016/j.addma.2021.102068.
[70] L. Liu, Q. Ding, Y. Zhong, J. Zou, J. Wu, Y.L. Chiu, J. Li, Z. Zhang, Q. Yu, Z. Shen, Dislocation network in additive manufactured steel breaks strength–ductility tradeoff, Mater, Today Off. 21 (2018) 354–361, https://doi.org/10.1016/j.mattod.2017.11.004.
[71] J. Liu, Y. Jin, X. Fang, C. Chen, Q. Feng, X. Liu, Y. Chen, T. Suo, F. Zhao, T. Huang, H. Wang, X. Wang, Y. Fang, Y. Wei, L. Meng, J. Lu, W. Yang, Dislocation strengthening without ductility trade-off in metastable austenitic steels, Sci. Rep. 6 (2016), 35345, https://doi.org/10.1038/srep35345.

[72] J. Pesicka, R. Kuzel, A. Dronhofer, G. Eggeler, The evolution of dislocation density during heat treatment and creep of tempered martensite ferritic steels, Acta Mater. 51 (2003) 4847–4862, https://doi.org/10.1016/S1359-6454(03)00324-0.
[73] D. Rojas, J. Garcia, O. Prat, L. Agudo, C. Carrasco, G. Sauthoff, a.R. Kaysser-Pyzalla, Effect of processing parameters on the evolution of dislocation density and subgrain size of a 12%Cr heat resistant steel during creep at 650°C, Mater. Sci. Eng. 528 (2011) 1372–1381, https://doi.org/10.1016/j.msea.2010.10.028.
[74] T. Malis, S.C. Cheng, R.F. Egerton, EELS log-ratio technique for specimen-thickness measurement in the TEM, J. Electron. Microsc. Tech. 8 (1988) 193–200, https://doi.org/10.1002/jemt.1060080206.
[75] D.N. Seidman, E.A. Marquis, D.C. Dunand, Precipitation strengthening at ambient and elevated temperatures of heat-treatable Al(Sc) alloys, Acta Mater. 50 (2002) 4021–4035, https://doi.org/10.1016/S1359-6454(02)00201-X.